Springer

KSME

Journal of Mechanical Science and Technology 31 (7) (2017) 3143~3155
www.springerlink.com/content/1738-494x(Print)/1976-3824(Online)
DOI 10.1007/s12206-017-0604-4

Dynamic analysis of an axially moving robot manipulator supported by bearings †

Jaewon Kim and Jintai Chung*

Department of Mechanical Engineering, Hanyang University, 55 Hanyangdaehak-ro, Sangnok-gu, Ansan, Gyeonggi-do 15588, Korea

(Manuscript Received August 2, 2016; Revised February 27, 2017; Accepted March 15, 2017)

Abstract

In this study, a robot manipulator is modelled as a cantilever beam, which moves in an axial direction, has a lumped mass at the end, and is supported by intermediate springs. Considering the tip mass and intermediate springs in the modeling, we derive the equations of motion in which the rigid-body motion is coupled with the flexible motions, and then analyze the transverse vibrations of the beam. Furthermore, we study the tip mass effects on the natural frequencies and the corresponding mode shapes. The natural frequency loci veering is analyzed for variations in the tip mass and the spring position/stiffness. In addition, we investigate the exchange and localization of modes around these veering regions as well as the parameter effects on the mode shapes. Using a Short-time Fourier transform (STFT), the relationship between the dynamic characteristics and dynamic responses are described. It is found that the dynamic characteristics of the beam are dependent on the veering distance. It is also shown via dynamic responses that the mode exchanges occur when a veering distance is close.

Keywords: Axially moving robot manipulator; Mode exchange; Tip mass effect; Natural frequency loci veering

1. Introduction

A robot manipulator moving in the axial direction can be modelled as an axially moving beam which is used in various industrial fields. These applications need dynamic analyses because the systems require high accuracy of positioning after moving. More realistic studies for dynamic models have been conducted for exact predictions of dynamic behavior and control.

Previous studies of axially moving beams related to this study can be classified into two categories. The first category includes studies of deploying or retracting beams, such as deployable space appendages, robot manipulators, and machine tools [1-14]. The second category includes axially moving beams with hinged end conditions, such as conveyor belts and band-saw blades [15-24]. These papers are described in more detail as follows.

Some studies in the first category examined the dynamic behavior when deploying or retracting a beam. Wang and Wei [1] analyzed the transverse vibration in a robot arm, modeled as a moving slender beam. They found that deploying and retracting motions show the effects of destabilizing and stabilizing on the transverse beam vibrations, respectively. Stylianou and Tabarrok [2] obtained a numerical solution for transverse displacement using a finite element analysis. In their paper, the dynamic response of the beam was investigated using various velocity profiles of the deploying and retracting motions. Wang et al. [3] analyzed the vibration of an axially translating beam featuring time-variant velocity. This study shows that the beam acceleration in the axial direction does not affect the stabilization of the transverse vibration. Matsuzaki et al. [4] compared a finite element method simulation and experimental results for bending oscillation when deploying or retrieving a beam. In Al-Bedoor and Khulief [5], an approximate analytical solution was presented for the transverse displacement of a flexible beam moving axially under various boundary conditions. Al-Bedoor and Khulief [6] also studied the transverse vibration of an axially translating beam with rotational motion. They considered the dynamic coupling terms between translation motion, rotation motion, and elastic deformation, and accounted for the stiffening effect of beam rotation. Zhu and Chung [7] found the beat phenomenon from lateral vibration of a deploying beam with spin. Fung et al. [8] derived the equations of motion for an axially moving beam using the Timoshenko beam theory, and Chang et al. [9] investigated the vibration and stability of an axially translating beam, based on the Rayleigh beam theory. Furthermore, Wang et al. [10] studied the dynamic response of an axially moving viscoelastic beam with varying length and axial velocity. Park et al. [11] obtained the governing vibration equations for a deploying or retracting beam using the von Karman strain theory. Longitudinal and transverse vibrations were analyzed regarding Young's modulus and axial moving

*Corresponding author. Tel.: +82 31 400 5287, Fax.: +82 31 406 6964
E-mail address: jchung@hanyang.ac.kr
† Recommended by Associate Editor Sungsoo Na

velocity/acceleration of the beam. Park et al. [12] also compared the governing equations and dynamic response derived from the Eulerian and Lagrangian descriptions. They proposed that the Lagrangian description should be selected for a deploying beam model because the Lagrangian equations are simpler than the Eulerian equations.

Studies for more targeted, specific applications have also been carried out. Duan et al. [13] studied the transverse vibration in a crane jib, modeled by an axially moving nested cantilever beam. Kim and Chung [14] considered a takeout robot, modeled by an axially moving flexible beam from a translating hub, and described vibration reduction for transverse vibrations.

The second category consists of studies on the dynamic responses and characteristics of axially moving beams with hinged end conditions. Ozkaya and Pakdemirli [15] presented the approximate solutions for a beam with harmonically varying velocity and exponentially decaying velocity. Yang et al. [16] derived a closed-form approximate solution to obtain the natural frequency of an axially moving beam. With both high moving speed and large bending stiffness, the solution obtained was valid and accurate. Rezaee and Lotfan [17] analyzed the natural frequency, complex mode shape, and response for an axially moving nanoscale beam considering the non-local theory. Additionally, the effects of intermediate support on the dynamic behaviors of an axially moving beam have been investigated. Pierre et al. [18] obtained the theoretical and experimental vibration mode of a disordered two-span beam with torsional spring. This paper showed that a small deviation in span lengths from an ideal value caused dramatic changes in the dynamic characteristics of a two-span beam. Pierre [19] analyzed the effects on disorder in vibration mode of periodic structures. They found that the natural frequency loci veering and strong localization of mode shape occurred with small structural irregularities. Lust et al. [20] investigated the influence of various effects on mode localization in multispan beams. They found that span length imperfections and transverse support stiffness are significant parameters for mode localization. Al-Jawi et al. [21] studied normal mode localization on stationary and axially moving disordered dual-span beams. The localization became stronger as the span axial tension increased in the stationary case, and as the transport speed increased in the axially moving case. Moreover, many studies related to the dynamic response and stability of moving beams with intermediate springs were published. Ghayesh [22] derived the governing equations of non-linear transverse vibration on an axially moving beam supported by an intermediate spring. The stability of the system was analyzed using amplitude-frequency response and bifurcation diagrams. Ghayesh et al. [23] investigated the stability of the coupled longitudinal and transverse vibrations with various parameters. They proposed that the spring location and stiffness were dominant factors with respect to the dynamics of the system. Jaiswal and Iyengar [24] studied the dynamic response of a beam resting on an elastic foundation under a moving force.

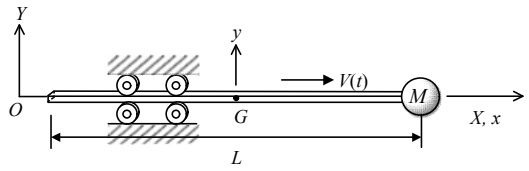

Fig. 1. Schematic of an axially moving robot manipulator.

Recently, a robot manipulator, modeled as an axially moving beam with spring supports, was studied by Park and Chung [25]. They observed the natural frequency loci veering of the beam with variation in the position/stiffness of springs, and investigated the characteristics of the mode shape in those veering regions. They also presented a reduction condition for the transverse vibration of the beam using mode localization. However, a robot manipulator generally translates the payload using the end effector of the robot arm, so many researchers have also considered a tip mass when modeling a payload [1, 6, 8, 13, 14]. As described in previous studies, the dynamic characteristics and dynamic behavior of a system are changed by the tip mass. To predict and control the dynamic analysis of a system, we should analyze the effects of a tip mass on a moving beam which is supported by springs.

This study investigates the effects of a tip mass, as well as spring position and spring constant, on the dynamic characteristics and the dynamic behavior of a moving finite-length beam with a tip mass and intermediate springs. The tip mass effect is considered in the equations for coupled rigid-body/flexible motions and the corresponding boundary conditions. After the equations of motion are transformed to weak forms, the weak forms are discretized using the Galerkin method. The natural frequencies and mode shapes of the beam are investigated by solving the eigenvalue problem. The dynamic responses of the axially moving beam with a tip mass are obtained using a generalized-alpha time integration method [26]. Using the Short-time Fourier transform (STFT), we describe the cause-and-effect relationship between the dynamic characteristics and dynamic behavior.

2. Equations of motion

A robot manipulator with a planar motion can be modeled by a moving beam with a tip mass which is supported by rollers, as shown in Fig. 1. If the manipulator has a three-dimensional motion in the space, it may exhibit more complicated dynamics than the manipulator with a planar motion. For this reason, the analysis of this study is restricted to a manipulator with a planar motion. A total length, cross-sectional area, area moment of inertia, Young's modulus and mass density are denoted by L, A, I, E and ρ, respectively. The moving speed of the beam is given by $V(t)$. A tip mass with mass M is attached to the right end of the beam. A dynamic model of the finite-length beam is shown in Fig. 2, where the tip mass is supposed to be a point mass, and rollers are modeled by the

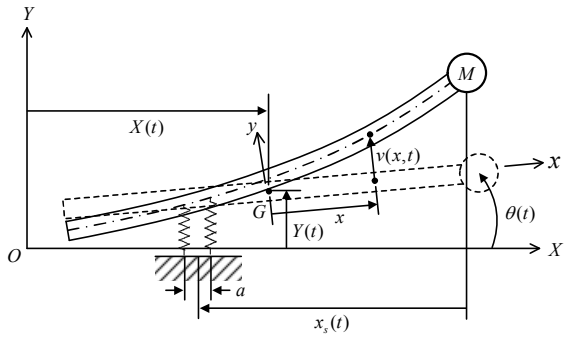

Fig. 2. Axially moving beam with a tip mass supported by springs.

springs k without a damper. In this study, it is assumed that the moving beam is modeled as an Euler-Bernoulli beam, and the springs deform only in the vertical direction. The distance from the tip mass to the midpoint between the two springs is $x_s(t)$, and the gap between the two springs, is a. The horizontal and vertical displacements for the center of gravity G of the beam are $X(t)$ and $Y(t)$, respectively, and the angular displacement for the rigid motion of the beam is $\theta(t)$. The beam has a distributed transverse force per unit length which is denoted by $p(x, t)$. The beam position due to only rigid-body motion is described by the dashed line, and the deformed beam due to both flexible and rigid-body motions is described as the solid line (Fig. 2). In this figure, the X-Y frame is an inertial reference frame, and the x-y frame is a body-fixed reference frame, which is attached to the beam. The transverse deflection of the beam is expressed by $v(x, t)$ in the x-y frame, and the longitudinal deflection is assumed to be small and negligible.

The position vector of a point at a distance x away from the beam gravity center G can be written as

$$\mathbf{r} = \left(X + x\cos\theta - v\sin\theta\right)\mathbf{I} + \left(Y + x\sin\theta + v\cos\theta\right)\mathbf{J} \tag{1}$$

where $\mathbf{I}$ is a unit vector in the X direction and $\mathbf{J}$ are a unit vector in the Y direction. The position vector for the tip mass, which is attached at the right end of the beam, is given by

$$\mathbf{r}_M = \left(X + \frac{L}{2}\cos\theta - v|_{x=L/2}\sin\theta\right)\mathbf{I} + \left(Y + \frac{L}{2}\sin\theta + v|_{x=L/2}\cos\theta\right)\mathbf{J} \tag{2}$$

where $v|_{x=L/2}$ is a transverse deflection at $x = L/2$. Similarly, the position vectors for the attached point of the springs on the beam are given by

$$\mathbf{r}_n = \left[X + \left(\frac{L}{2} - x_n\right)\cos\theta - v|_{x=L/2-x_n}\sin\theta\right]\mathbf{I} + \left[Y + \left(\frac{L}{2} - x_n\right)\sin\theta + v|_{x=L/2-x_n}\cos\theta\right]\mathbf{J} \quad \text{for } n = 1,2 \tag{3}$$

where x_n is the distance from the tip mass to the n^{th} spring, as shown in Fig. 2, and $v|_{x=L/2-x_n}$ is the transverse deflection of the beam at the n^{th} spring position. The speed in the horizontal direction for the center of gravity G is the same as the axially moving speed: i.e., $\dot{X}(t) = V(t)$. The velocity vectors for a point on the beam and the tip mass, denoted by $\mathbf{v}$ and $\mathbf{v}_M$, respectively, are obtained by differentiation of the position vector with respect to time, as follows:

$$\mathbf{v} = \left[V - \left(x\dot{\theta} + \frac{\partial v}{\partial t}\right)\sin\theta - v\dot{\theta}\cos\theta\right]\mathbf{I} + \left[\dot{Y} + \left(x\dot{\theta} + \frac{\partial v}{\partial t}\right)\cos\theta - v\dot{\theta}\sin\theta\right]\mathbf{J} \tag{4}$$

$$\mathbf{v}_M = \left[V - \left(\frac{L}{2}\dot{\theta} + \left.\frac{\partial v}{\partial t}\right|_{x=L/2}\right)\sin\theta - v|_{x=L/2}\dot{\theta}\cos\theta\right]\mathbf{I} + \left[\dot{Y} + \left(\frac{L}{2}\dot{\theta} + \left.\frac{\partial v}{\partial t}\right|_{x=L/2}\right)\cos\theta - v|_{x=L/2}\dot{\theta}\sin\theta\right]\mathbf{J}\,. \tag{5}$$

The kinetic energy can be obtained from the velocity vectors and can be written as

$$T = \frac{1}{2}\rho A\int_{-L/2}^{L/2}\mathbf{v}\cdot\mathbf{v}\,\mathrm{d}x + \frac{1}{2}M\,\mathbf{v}_M\cdot\mathbf{v}_M\,. \tag{6}$$

The linear equations of motion of the axially moving beam with a tip mass supported by springs can be derived using a similar derivation process to that described in Ref. [25]. The difference between this study and Ref. [25] is considering structural damping of the beam, which is denoted by c_d.

To generalize the discussion, dimensionless equations of motion are required and the following dimensionless parameters are defined:

$$t^* = \sqrt{\frac{EI}{\rho AL^4}}t,\ x^* = \frac{x}{L},\ x_s^* = \frac{x_s}{L},\ Y^* = \frac{Y}{L},\ v^* = \frac{v}{L},\ a^* = \frac{a}{L},$$
$$k^* = \frac{kL^3}{EI},\ M^* = \frac{M}{\rho AL},\ p^* = \frac{pL^3}{EI},\ V^* = V\sqrt{\frac{\rho AL^2}{EI}},$$
$$c_d^* = \frac{c_d L}{\sqrt{\rho AEI}}\,. \tag{7}$$

Using the dimensionless parameters and dropping the asterisks, the dimensionless equations are derived and can be written as:

$$\ddot{Y} + \frac{\partial^2 v}{\partial t^2} + M\left(\ddot{Y} + x\ddot{\theta} + \frac{\partial^2 v}{\partial t^2}\right)\delta\left(x - \frac{1}{2}\right) + \sum_{n=1}^{2}k\left(Y + x\theta + v\right)\delta\left(x - \frac{1}{2} + x_n\right) = p \tag{8}$$

$$\frac{1}{12}\ddot{\theta} + x\frac{\partial^2 v}{\partial t^2} - \dot{V}v + M\left[x\left(\ddot{Y} + x\ddot{\theta} + \frac{\partial^2 v}{\partial t^2} - \dot{V}\theta\right) - \dot{V}v\right]\delta\left(x - \frac{1}{2}\right)$$

$$+\sum_{n=1}^{2} kx\left(Y+x\theta+v\right)\delta\left(x-\frac{1}{2}+x_n\right)=px \tag{9}$$

$$\ddot{Y}+\frac{\partial^2 v}{\partial t^2}-\dot{V}\theta+\frac{\partial^4 v}{\partial x^4}+c_d\frac{\partial v}{\partial t}$$
$$+\sum_{n=1}^{2} k\left(Y+x\theta+v\right)\delta\left(x-\frac{1}{2}+x_n\right)=p \tag{10}$$

where $\delta(x)$ is a Dirac delta function. The dimensionless boundary conditions are

$$\frac{\partial^2 v}{\partial x^2}=\frac{\partial^3 v}{\partial x^3}=0 \quad \text{at } x=-\frac{1}{2} \tag{11}$$

$$\frac{\partial^2 v}{\partial x^2}=0,\ \frac{\partial^3 v}{\partial x^3}=M\left(\ddot{Y}+x\ddot{\theta}+\frac{\partial^2 v}{\partial t^2}-\dot{V}\theta\right) \quad \text{at } x=\frac{1}{2}. \tag{12}$$

Eqs. (8) and (9) represent the rigid-body motion for Y and θ, respectively. Eq. (10) is the flexible motion for the transverse deflection v. These three equations are coupled with each other. Compared with Ref. [25], these equations have new terms, corresponding to the tip mass. The third term in Eq. (8) and the fourth term in Eq. (9) represent the inertia force caused by the tip mass, and the second equation in Eq. (12) is the boundary condition in which the inertia force of the tip mass is equal to the shear force at the beam's right end.

3. Discretized equations

The Galerkin method is utilized to discretize the equations of motion. Before using the Galerkin method, the weak forms are derived from the partial differential equations and boundary conditions. Trial and weighting functions are required to derive the weak forms. The trial functions are denoted by Y, θ and v, and the corresponding weighting functions are denoted by $\overline{Y}$, $\overline{\theta}$ and $\overline{v}$, respectively. $\overline{Y}$ and $\overline{\theta}$ are functions for the time and $\overline{v}$ is a function for the position and time. The weak forms are obtained by multiplying Eqs. (8)-(10) by the corresponding weighting functions, and integrating the resulting equation over the beam domain. The following weak form for v considers the natural boundary condition of the shear force.

$$\ddot{Y}+\int_{-1/2}^{1/2}\frac{\partial^2 v}{\partial t^2}\mathrm{d}x+M\left(\ddot{Y}+x\ddot{\theta}+\frac{\partial^2 v}{\partial t^2}\right)\delta\left(x-\frac{1}{2}\right)$$
$$+\sum_{n=1}^{2} k\left(Y+x\theta+v\right)\delta\left(x-\frac{1}{2}+x_n\right)=\int_{-1/2}^{1/2} p\,\mathrm{d}x \tag{13}$$

$$\frac{1}{12}\ddot{\theta}+\int_{-1/2}^{1/2} x\frac{\partial^2 v}{\partial t^2}\mathrm{d}x-\int_{-1/2}^{1/2}\dot{V}v\,\mathrm{d}x$$
$$+M\left[x\left(\ddot{Y}+x\ddot{\theta}+\frac{\partial^2 v}{\partial t^2}-\dot{V}\theta\right)-\dot{V}v\right]\delta\left(x-\frac{1}{2}\right)$$
$$+\sum_{n=1}^{2} kx\left(Y+x\theta+v\right)\delta\left(x-\frac{1}{2}+x_n\right)=\int_{-1/2}^{1/2} p\,x\,\mathrm{d}x \tag{14}$$

$$\int_{-1/2}^{1/2}\overline{v}\,\ddot{Y}\,\mathrm{d}x+\int_{-1/2}^{1/2}\overline{v}\frac{\partial^2 v}{\partial t^2}\mathrm{d}x-\int_{-1/2}^{1/2}\overline{v}\,\dot{V}\theta\,\mathrm{d}x+\int_{-1/2}^{1/2}\frac{\partial\overline{v}}{\partial x^2}\frac{\partial v}{\partial x^2}\mathrm{d}x$$
$$+\int_{-1/2}^{1/2}\overline{v}c_d\frac{\partial v}{\partial t}\mathrm{d}x+\overline{v}\,M\left(\ddot{Y}+x\ddot{\theta}+\frac{\partial^2 v}{\partial t^2}-\dot{V}\theta\right)\delta\left(x-\frac{1}{2}\right)$$
$$+\sum_{n=1}^{2}\overline{v}\,k\left(Y+x\theta+v\right)\delta\left(x-\frac{1}{2}+x_n\right)=\int_{-1/2}^{1/2}\overline{v}\,p\ \mathrm{d}x\,. \tag{15}$$

The trial and weighting functions for transverse motion can be approximated by linear combinations of basis functions,

$$v(x,t)=\sum_{j=1}^{J} T_j(t)V_j(x),\quad \overline{v}(x,t)=\sum_{i=1}^{J}\overline{T}_i(t)V_i(x) \tag{16}$$

where V_j are the basis functions, T_j are unknown functions of time, $\overline{T}_i$ are arbitrary functions of time, and J is the number of the functions. Note that the comparison functions satisfy both the essential and natural boundary conditions while the admissible functions satisfy only the essential boundary condition. It is difficult to select the comparison functions satisfying the natural boundary condition for the shear force at the beam end. Thus, the admissible functions, which are easier to select than the comparison functions, are used as the basis functions in this study. It is reasonable to use the admissible functions because the natural boundary conditions have already been applied during derivation of the weak form for transverse motion. In this study, the mode functions for the transverse vibration of a beam with free-free boundary conditions are selected as the basis function and written as

$$V_j(x)=\cosh\beta_j\left(x+\frac{1}{2}\right)+\cos\beta_j\left(x+\frac{1}{2}\right)$$
$$-\frac{\cosh\beta_j-\cos\beta_j}{\sinh\beta_j-\sin\beta_j}\left[\sinh\beta_j\left(x+\frac{1}{2}\right)+\sin\beta_j\left(x+\frac{1}{2}\right)\right] \tag{17}$$

where x ranges from -1/2 to 1/2, and β_j is the j^{th} root of the following frequency equation:

$$\cosh\beta_j\cdot\cos\beta_j=1\,. \tag{18}$$

The discretized equations are obtained by substituting the trial and weighting functions of Eq. (16) into Eqs. (13)-(15). The discretized equations for Y, θ and v are expressed as

$$(1+M)\ddot{Y}+\frac{1}{2}M\ddot{\theta}+\sum_{j=1}^{J} m_{Yj}\ddot{T}_j$$
$$+2kY+\left(1-2x_s\right)k\theta+\sum_{j=1}^{J} k_{Yj}T_j=f_Y \tag{19}$$

$$\frac{1}{2}M\ddot{Y}+\left(\frac{1}{12}+\frac{1}{4}M\right)\ddot{\theta}+\sum_{j=1}^{J} m_{\theta j}\ddot{T}_j+\left(1-2x_s\right)kY$$
$$+\frac{1}{2}\left[k(4x_s^{\,2}+a^2+1-4x_s)-M\dot{V}\right]\theta$$

$$+\sum_{j=1}^{J}\left(k_{\theta j}-\dot{V}m_{Yj}\right)T_j=f_\theta \tag{20}$$

$$m_{iY}\ddot{Y}+m_{i\theta}\ddot{\theta}+\sum_{j=1}^{J}(\delta_{ij}+m_{ij})\ddot{T}_j+\sum_{j=1}^{J}\left(c_d\delta_{ij}\right)\dot{T}_j+k_{iY}Y$$
$$+\left(k_{i\theta}-\dot{V}m_{iY}\right)\theta+\sum_{j=1}^{J}\left(\beta_i^4\delta_{ij}+k_{ij}\right)T_j=f_v \tag{21}$$

where

$$m_{Yj}=MV_j\left(\frac{1}{2}\right),\ m_{\theta j}=\frac{1}{2}MV_j\left(\frac{1}{2}\right),\ m_{iY}=MV_i\left(\frac{1}{2}\right),$$
$$m_{i\theta}=\frac{1}{2}MV_i\left(\frac{1}{2}\right),\ m_{ij}=\sum_{j=1}^{J}MV_i\left(\frac{1}{2}\right)V_j\left(\frac{1}{2}\right),$$
$$k_{Yj}=\sum_{n=1}^{2}kV_j\left(\frac{1}{2}-x_n\right),\ k_{\theta j}=\sum_{n=1}^{2}k\left(\frac{1}{2}-x_n\right)V_j\left(\frac{1}{2}-x_n\right),$$
$$k_{iY}=\sum_{n=1}^{2}kV_i\left(\frac{1}{2}-x_n\right),\ k_{i\theta}=\sum_{n=1}^{2}k\left(\frac{1}{2}-x_n\right)V_i\left(\frac{1}{2}-x_n\right),$$
$$k_{ij}=\sum_{n=1}^{2}kV_i\left(\frac{1}{2}-x_n\right)V_j\left(\frac{1}{2}-x_n\right),\ f_Y=\int_{-1/2}^{1/2}p\,\mathrm{d}x,$$
$$f_\theta=\int_{-1/2}^{1/2}px\,\mathrm{d}x,\ f_v=\int_{-1/2}^{1/2}pV_i(x)\mathrm{d}x\,. \tag{22}$$

The discretized equations are expressed by a matrix-vector equation, as follows:

$$\begin{bmatrix} m_Y & m_{Y\theta} & \mathbf{m}_{Yv} \\ m_{\theta Y} & m_\theta & \mathbf{m}_{\theta v} \\ \mathbf{m}_{vY} & \mathbf{m}_{v\theta} & \mathbf{m}_v \end{bmatrix}\begin{Bmatrix} \ddot{Y} \\ \ddot{\theta} \\ \ddot{\mathbf{T}}_v \end{Bmatrix}+\begin{bmatrix} 0 & 0 & \mathbf{0} \\ 0 & 0 & \mathbf{0} \\ \mathbf{0} & \mathbf{0} & \mathbf{c}_v \end{bmatrix}\begin{Bmatrix} \dot{Y} \\ \dot{\theta} \\ \dot{\mathbf{T}}_v \end{Bmatrix}$$
$$+\begin{bmatrix} k_Y & k_{Y\theta} & \mathbf{k}_{Yv} \\ k_{\theta Y} & k_\theta & \mathbf{k}_{\theta v} \\ \mathbf{k}_{vY} & \mathbf{k}_{v\theta} & \mathbf{k}_v \end{bmatrix}\begin{Bmatrix} Y \\ \theta \\ \mathbf{T}_v \end{Bmatrix}=\begin{Bmatrix} f_Y \\ f_\theta \\ \mathbf{f}_v \end{Bmatrix} \tag{23}$$

where

$$m_Y=1+M,\ m_{Y\theta}=m_{\theta Y}=\frac{M}{2},\ m_\theta=\frac{3M+1}{12},\ k_Y=2k,$$
$$k_{Y\theta}=k_{\theta Y}=(1-2x_s)k,\ k_\theta=\frac{1}{2}\left[k(4x_s^{\,2}+a^2+1-4x_s)-M\dot{V}\right],$$
$$\mathbf{m}_{Yv}=\left\{m_{Yj}\right\}^{\mathrm{T}},\ \mathbf{m}_{\theta v}=\left\{m_{\theta j}\right\}^{\mathrm{T}},\ \mathbf{m}_{vY}=\left\{m_{iY}\right\},$$
$$\mathbf{m}_{v\theta}=\left\{m_{i\theta}\right\},\ \mathbf{m}_v=\left[\sum_{j=1}^{J}\left(\delta_{ij}+m_{ij}\right)\right],\ \mathbf{k}_{Yv}=\left\{k_{Yj}\right\}^{\mathrm{T}},$$
$$\mathbf{k}_{\theta v}=\left\{k_{\theta j}-\dot{V}m_{Yj}\right\}^{\mathrm{T}},\ \mathbf{k}_{vY}=\left\{k_{iY}\right\},\ \mathbf{k}_{v\theta}=\left\{k_{i\theta}-\dot{V}m_{iY}\right\},$$
$$\mathbf{k}_v=\left[\sum_{j=1}^{J}\left(\beta_i^4\delta_{ij}+k_{ij}\right)\right],\ \mathbf{c}_v=\sum_{j=1}^{J}\left(c_d\delta_{ij}\right),\ \mathbf{f}_v=\left\{f_v\right\}. \tag{24}$$

4. Natural frequencies

Convergence tests for the natural frequency of the stationary beam are performed to determine a suitable number of basis functions for computation. Convergence tests can be performed for two cases - the tip mass does not exist and does exist - because the characteristics of the basis function and mass matrix change with the tip mass. When the tip mass does not exist, convergence tests are carried out according to Park and Chung [25], where it was shown that 25 basis functions are suitable. In this study, when the tip mass exists, convergence tests are carried out for the dimensionless spring position, x_s = 0.025 and 0.5. For convenience, the dimensionless natural frequency is defined as $\lambda_n=\omega_n\sqrt{\rho AL^4/EI}$ where ω_n is the natural frequency. Note that structural damping is neglected, i.e., c_d = 0, when analyzing the natural frequencies and mode shapes.

Table 1. Natural frequency convergence characteristics when the stationary beam has M = 0.4, k = 30 × 10^3, a = 0.05 and x_s = 0.025.

Number of basis functions (J)	Dimensionless natural frequencies (λ_n)					
	λ_1	λ_2	λ_3	λ_4	λ_5	λ_6
1	1.4607	35.986	43.507	-	-	-
2	1.4479	7.9112	38.330	43.507	-	-
3	1.4471	7.4820	12.542	40.494	59.176	-
4	1.4459	7.4276	12.496	28.342	41.581	59.345
5	1.4426	7.4261	12.428	27.060	35.328	42.413
6	1.4423	7.4141	12.420	26.852	35.253	42.347
7	1.4423	7.3933	12.343	26.850	35.038	42.085
8	1.4422	7.3892	12.340	26.785	35.021	42.061
9	1.4418	7.3890	12.333	26.646	34.786	42.056
10	1.4418	7.3872	12.331	26.618	34.779	42.047
11	1.4418	7.3835	12.318	26.618	34.743	42.003
12	1.4418	7.3835	12.318	26.618	34.743	42.003
13	1.4418	7.3831	12.314	26.610	34.709	41.994
14	1.4418	7.3831	12.314	26.610	34.709	41.994
15	1.4417	7.3829	12.312	26.606	34.689	41.989
16	1.4417	7.3829	12.312	26.606	34.689	41.989
17	1.4417	7.3828	12.310	26.604	34.677	41.987
18	1.4417	7.3828	12.310	26.604	34.677	41.987
19	1.4417	7.3827	12.309	26.602	34.669	41.985
20	1.4417	7.3827	12.309	26.602	34.669	41.985
21	1.4417	7.3826	12.309	26.601	34.663	41.983
22	1.4417	7.3826	12.309	26.601	34.663	41.983
23	1.4417	7.3825	12.308	26.599	34.656	41.982
24	1.4417	7.3825	12.308	26.599	34.656	41.982
25	1.4417	7.3825	12.308	26.599	34.656	41.982

In Tables 1 and 2, the convergence characteristics of the natural frequencies are shown for x_s = 0.025 and 0.5, when M = 0.4, k = 30 × 10^3, a = 0.05 and p = 0. As shown in Tables 1 and 2, the natural frequencies converge to J = 25. Thus, 25 basis functions are suitable for computation regardless of the tip mass value. These values are applied in further computations in this paper.

The natural frequencies for a stationary beam with a tip

Table 2. Natural frequency convergence characteristics when the stationary beam has $M = 0.4$, $k = 30 \times 10^3$, $a = 0.05$ and $x_s = 0.5$.

Number of basis functions (J)	Dimensionless natural frequencies (λ_n)					
	λ_1	λ_2	λ_3	λ_4	λ_5	λ_6
1	1.2894	3.0227	58.675	-	-	-
2	1.0867	2.2744	13.016	59.373	-	-
3	1.0867	2.2653	11.240	14.508	81.065	-
4	1.0625	2.1848	10.191	13.893	35.133	81.285
5	1.0613	2.1833	10.191	13.799	33.038	38.645
6	1.0432	2.1535	10.127	13.648	31.353	38.394
7	1.0432	2.1533	10.088	13.611	31.348	38.199
8	1.0365	2.1376	9.9604	13.562	31.316	38.023
9	1.0364	2.1375	9.9601	13.557	31.177	37.898
10	1.0310	2.1289	9.9357	13.520	30.921	37.863
11	1.0280	2.1289	9.9306	13.516	30.917	37.850
12	1.0280	2.1234	9.9036	13.497	30.854	37.816
13	1.0260	2.1234	9.9033	13.496	30.852	37.808
14	1.0260	2.1198	9.8858	13.484	30.812	37.787
15	1.0247	2.1198	9.8857	13.484	30.812	37.785
16	1.0247	2.1175	9.8742	13.476	30.786	37.771
17	1.0238	2.1175	9.8742	13.476	30.785	37.771
18	1.0238	2.1159	9.8664	13.471	30.768	37.762
19	1.0232	2.1159	9.8664	13.471	30.768	37.762
20	1.0232	2.1149	9.8613	13.468	30.757	37.756
21	1.0232	2.1149	9.8613	13.468	30.757	37.756
22	1.0226	2.1139	9.8558	13.465	30.744	37.752
23	1.0226	2.1139	9.8558	13.465	30.744	37.752
24	1.0225	2.1137	9.8553	13.464	30.743	37.749
25	1.0225	2.1137	9.8553	13.464	30.743	37.749

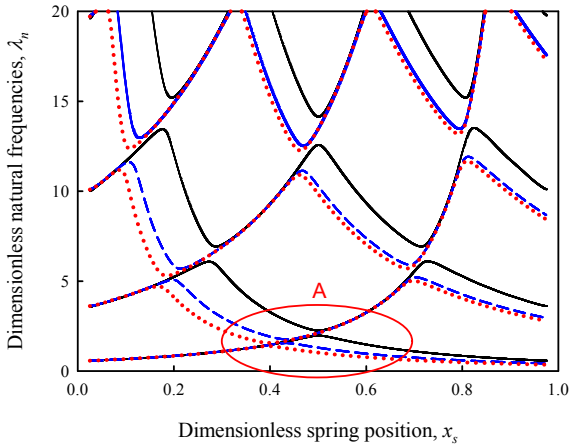

Fig. 3. Natural frequencies of a beam with a tip mass for variation in the spring position: $M = 0$ (solid line), $M = 0.2$ (dashed line), and $M = 0.4$ (dotted line).

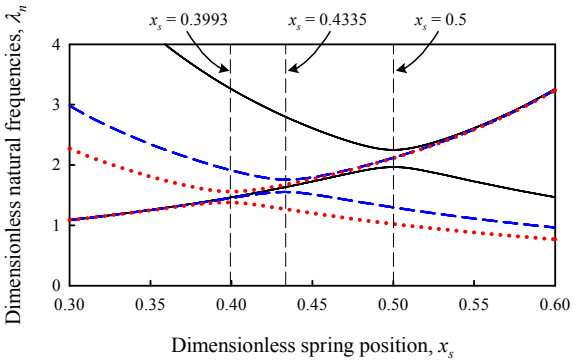

Fig. 4. Magnified plot of region A in Fig. 3: $M = 0$ (solid line), $M = 0.2$ (dashed line), and $M = 0.4$ (dotted line).

mass supported by springs are investigated for variation in the spring position/constant and tip mass. When the value of the dimensionless spring constant is fixed at $k = 30 \times 10^3$, and the dimensionless spring gap is given by $a = 0.05$, the natural frequency of the beam for the variation of the tip mass M and spring position x_s is analyzed. With three values of the dimensionless tip mass, $M = 0$, 0.2 and 0.4, the lowest four natural frequencies versus the spring position are shown in Fig. 3. In this figure, the solid, dashed and dotted lines stand for the natural frequencies for $M = 0$, 0.2 and 0.4, respectively. The solid line for $M = 0$ (i.e., the tip mass does not exist) are symmetric with respect to the spring position $x_s = 0.5$, while the dashed and dotted lines for $M = 0.2$ and 0.4 are not symmetric with respect to $x_s = 0.5$, and these lines will be further away from symmetric as the M value increases.

The natural frequency loci veering is analyzed for the natural frequencies when the spring is at a specific position (Fig. 3). Because the low mode of the beam is dominant in the behavior of the axially moving beam, the analysis focuses on the natural frequencies for the two lowest modes. Region A, shown in Fig. 3, which represents the veering of the first and second natural frequencies, is magnified to show the veering phenomenon clearly, and plotted in Fig. 4. In this figure, it is observed for $M = 0$, 0.2 and 0.4 that the natural frequencies veer at dimensionless spring positions $x_s = 0.5$, 0.4335 and 0.3993, respectively, and at these veering positions, the veering distance (gap between the two natural frequencies) decreases with the tip mass. By comparing the values of tip mass and the corresponding spring positions for veering, when the tip mass value increases, the value of the spring position for veering decreases (i.e., the spring position for veering shifts towards the tip mass position). To generalize the discussion of the shift effect, the effect of the tip mass on the veering position is presented in Fig. 5, where the veering positions for the tip mass $M = 0$, 0.2 and 0.4 correspond to those shown in Fig. 4, and the veering positions for the tip mass $M = 0.6$, 0.8 and 1.0 are computed similarly. As shown in this figure, as the value of M increases, the veering position shifts towards the tip mass position, and converges to a constant value.

It is valuable to investigate the characteristics of the veering phenomenon with variation in the spring constant k and the spring position x_s when $M = 0.2$ and $a = 0.05$. For three values of the dimensionless spring constant $k = 3 \times 10^3$, $k = 30 \times 10^3$

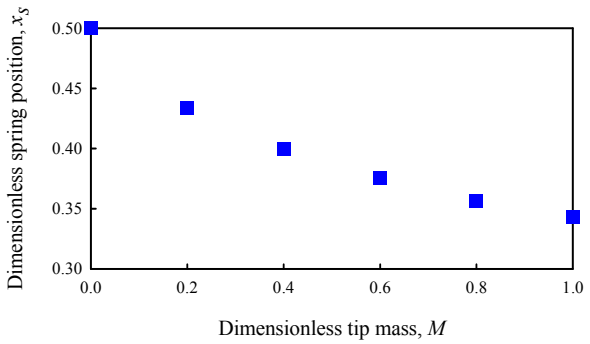

Fig. 5. Spring position at which the first and second natural frequencies veer for variation in the tip mass.

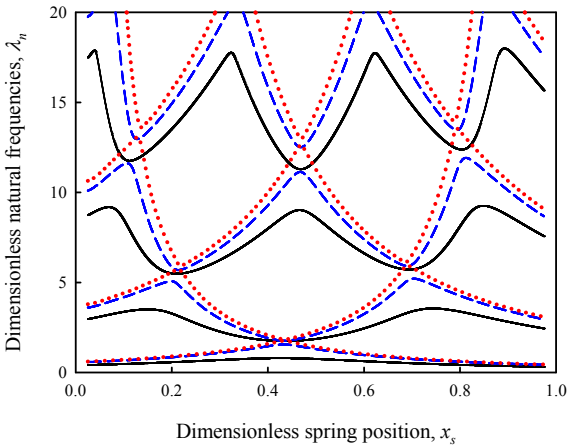

Fig. 6. Natural frequencies of a beam when $M = 0.2$ and $a = 0.05$: $k = 3 \times 10^3$ (solid line), $k = 30 \times 10^3$ (dashed line), and $k = 300 \times 10^3$ (dotted line).

and $k = 300 \times 10^3$, the dimensionless natural frequencies versus the dimensionless spring position are shown in Fig. 6. In this figure, the solid, dashed, and dotted lines stand for the natural frequencies when $k = 3 \times 10^3$, $k = 30 \times 10^3$ and $k = 300 \times 10^3$, respectively. It can be seen that as the spring constant increases, the veering distance decreases, while the veering positions hardly change.

The natural frequencies of first and second modes with variation of the tip mass M and the spring constant k are analyzed for a specific spring position x_s, where veering of the first and second natural frequencies is observed. When the dimensionless spring position $x_s = 0.5$, the two lowest natural frequencies versus the spring constant are illustrated in Fig. 7. As shown in Fig. 7(a), when $M = 0$, by magnifying the circle region, it is seen that the lines of two natural frequencies do not cross but veer for a specific spring constant, while the lines of the two natural frequencies for $M = 0.2$ or 0.4, shown in Figs. 7(b) and (c), do not veer. When we decrease the spring position x_s to 0.4335, the first and second natural frequencies for the spring constant, when $M = 0$, 0.2 and 0.4, are plotted in Figs. 8(a)-(c), respectively. As shown in Fig. 8, the natural frequency loci veering occurs for a beam with a tip

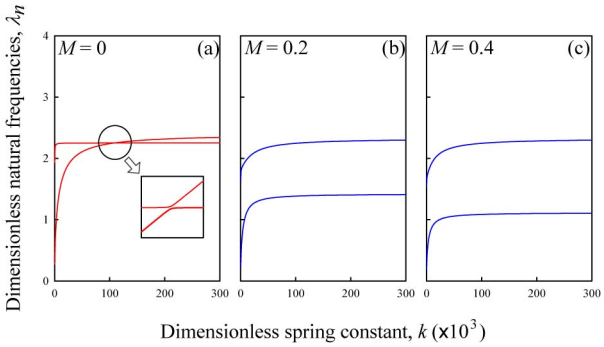

Fig. 7. Two lowest natural frequencies versus the spring constant when $x_s = 0.5$: (a) $M = 0$; (b) $M = 0.2$; (c) $M = 0.4$.

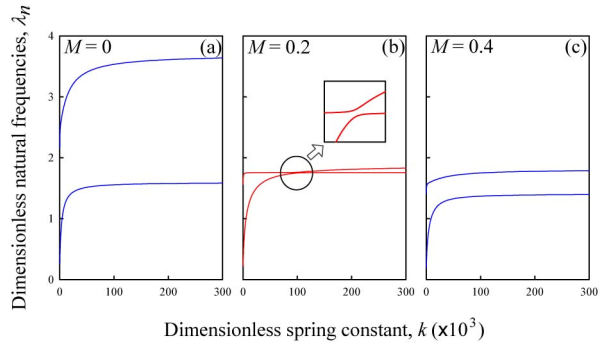

Fig. 8. Two lowest natural frequencies versus the spring constant when $x_s = 0.4335$: (a) $M = 0$; (b) $M = 0.2$; (c) $M = 0.4$.

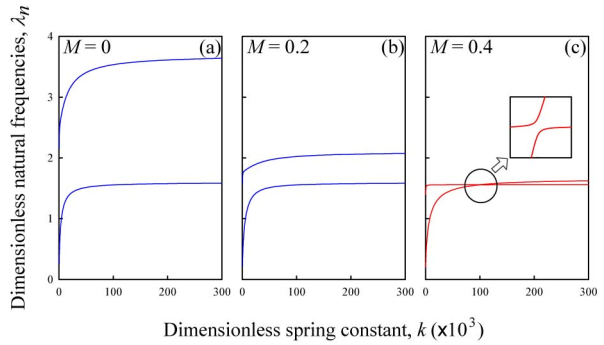

Fig. 9. First and second natural frequencies for variation in the spring constant when $x_s = 0.3993$: (a) $M = 0$; (b) $M = 0.2$; (c) $M = 0.4$.

mass $M = 0.2$ and spring position $x_s = 0.4335$, whereas the veering does not occur for $M = 0$ or 0.4. Similarly, for spring position $x_s = 0.3993$, the plots of natural frequencies versus the spring constant with a tip mass $M = 0$, 0.2 and 0.4 are plotted in Figs. 9(a)-(c), respectively. In this figure, the veering occurs in Fig. 9(c) for the specific spring constant when $x_s = 0.3993$ and $M = 0.4$.

The first and second natural frequencies for the variation of the tip mass are plotted in Fig. 10, when the dimensionless spring constant is $k = 30 \times 10^3$ and the dimensionless gap of the two springs is $a = 0.05$. Figs. 10(a)-(c) are plotted for the dimensionless spring position $x_s = 0.5$, 0.4335 and 0.3993, respectively. It can be seen that the two natural frequencies are

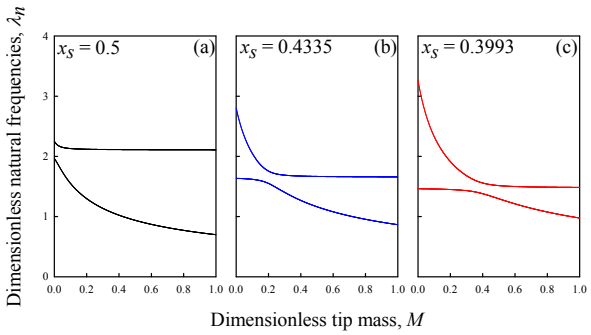

Fig. 10. First and second natural frequencies for variation in the tip mass when $k = 30 \times 10^3$: (a) $x_s = 0.5$; (b) $x_s = 0.4335$; (c) $x_s = 0.3993$.

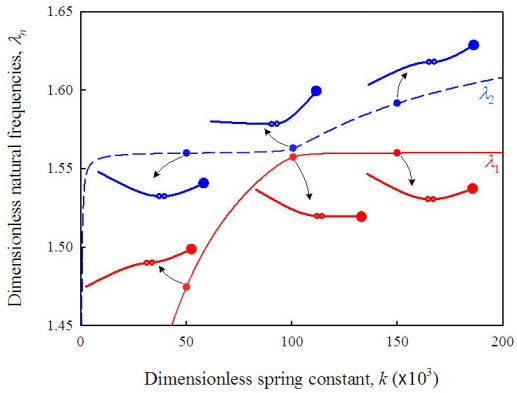

Fig. 11. First and second mode shapes around the veering region for variation in the spring constant when $M = 0.4$, $x_s = 0.3993$, and $a = 0.05$.

close for $M = 0$ and $x_s = 0.5$ in Fig. 10(a), $M = 0.2$ and $x_s = 0.4335$ in Fig. 10(b), and $M = 0.4$ and $x_s = 0.3993$ in Fig. 10(c), respectively. Consequently, the natural frequency veering is influenced by the spring position, spring constant, and tip mass.

5. Mode shapes

The first and second mode shapes around the veering region are analyzed next. First, the veering observed in Fig. 9(c) is magnified in Fig. 11, which represents the natural frequencies versus the spring constant. In this figure, the solid line represents the first dimensionless natural frequency and the dashed line is the second dimensionless natural frequency, and the mode shapes are plotted for the dimensionless spring constant $k = 50 \times 10^3$, 100.6×10^3 and 150×10^3. In the mode shapes, the large solid circle represents the tip mass and the two small hollow circles on the beam represent the springs. Based on the spring positions, the beam can be divided into left and right spans. For the spring constant $k = 100.6 \times 10^3$, it is observed that the two lowest natural frequencies are close, and one span has a large deflection while the other span has almost zero deflection; this indicates that the localization phenomenon of mode shapes occurs. In contrast, for $k = 50 \times 10^3$ and 150×10^3, both spans of the mode shapes have large deflections.

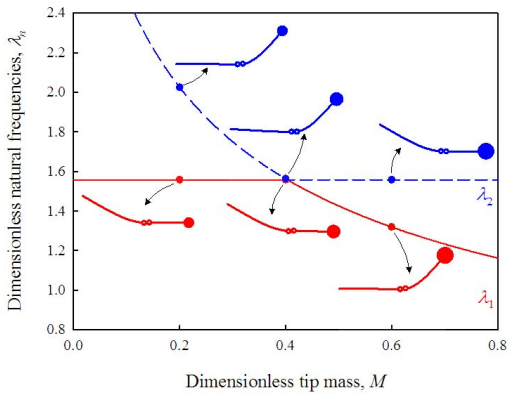

Fig. 12. First and second mode shapes around the veering region for variation in the tip mass when $k = 100.6 \times 10^3$, $x_s = 0.3993$, and $a = 0.05$.

Another observation is that the first mode shape for $k = 50 \times 10^3$ is similar to the second mode shape for $k = 150 \times 10^3$, while the second mode shape for $k = 50 \times 10^3$ is the similar to the first mode shape for $k = 150 \times 10^3$. This corresponds to the mode exchange phenomenon.

Next, the effects of the tip mass on the first and second mode shapes around the veering region are analyzed for the specific dimensionless spring constant $k = 100.6 \times 10^3$, which cause the mode localization shown in Fig. 11. When $x_s = 0.3993$ and $a = 0.05$, the first and second dimensionless natural frequencies for the variation in the dimensionless tip mass and the mode shapes corresponding to $M = 0.2$, 0.4 and 0.6 are plotted in Fig. 12, where the solid and dashed lines represent the first and second natural frequencies, respectively, and the size of the solid circle on the beam's right end is illustrated in proportion to the tip mass value. In this figure, at the point of $M = 0.4$, the lines of the natural frequencies of the first and second modes might appear to cross; however, in fact, they are extremely close at this point; therefore, these lines veer with each other rather than cross. Similar to the case shown in Fig. 11, the mode shapes exchange due to the veering and the mode shapes are localized. Mode localization occurs for $M = 0.2$, 0.4 and 0.6, which means that the mode localization here is not affected by the tip mass, for the specific spring constant value $k = 100.6 \times 10^3$.

For $k = 100.6 \times 10^3$, $M = 0.4$ and $a = 0.05$, the natural frequencies and mode shapes of the first and second modes when the spring position varies are plotted in Fig. 13. In this figure, around $x_s = 0.3993$, the two lowest natural frequencies veer and the corresponding mode shapes exchange, similar to Fig. 12. Note that for the specific spring constant $k = 100.6 \times 10^3$, the mode localization occurs for the dimensionless spring position $x_s = 0.34$, 0.3993 and 0.46; thus, the mode localization is not affected by the spring position.

Finally, when the tip mass and gap between the two springs are fixed at $M = 0.4$ and $a = 0.05$, we reduce the spring constant value and investigate its effect on the natural frequencies and mode shapes. Another two cases for dimensionless spring constant values are considered: Fig. 14 is for $k = 30 \times 10^3$ and

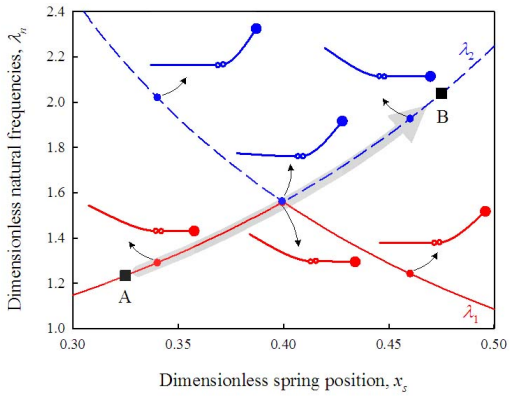

Fig. 13. First and second mode shapes around the veering region for variation in the spring position when $M = 0.4$, $k = 100.6 \times 10^3$, and $a = 0.05$.

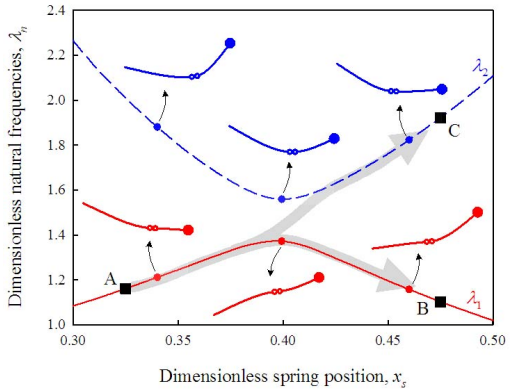

Fig. 14. First and second mode shapes around the veering region for variation in the spring position when $M = 0.4$, $k = 30 \times 10^3$, and $a = 0.05$.

Fig. 15 is for $k = 3 \times 10^3$. Comparing the dimensionless natural frequencies shown in Figs. 13-15, it is observed that the natural frequencies are reduced and this is reasonable because the overall stiffness of the system decreases. Another observation is that the veering distance around $x_s = 0.3993$ in Figs. 13 and 14 increases as the spring constant value decreases, while in Fig. 15, the first and second natural frequencies become further away due to the small spring constant; thus, no veering phenomenon occurs in Fig. 15. Due to the disappearance of veering, the mode shapes do not exchange in Fig. 15. It is observed in Fig. 14 that as the spring constant decreases for $k = 30 \times 10^3$, the mode localization becomes weak at $x_s = 0.34$ and 0.46, while mode localization does not occur at $x_s = 0.3993$. In Fig. 15, because the spring constant becomes rather small, mode localization also does not occur. Consequently, mode localization and mode exchange are closely related to the natural frequency veering.

6. Time responses

The dynamic responses for the transverse vibration at the two ends of the beam are analyzed next. Consider the motion of the axially moving beam in Fig. 16. The beam is initially located on the left side of the spring position, as shown in Fig. 16(a), and it

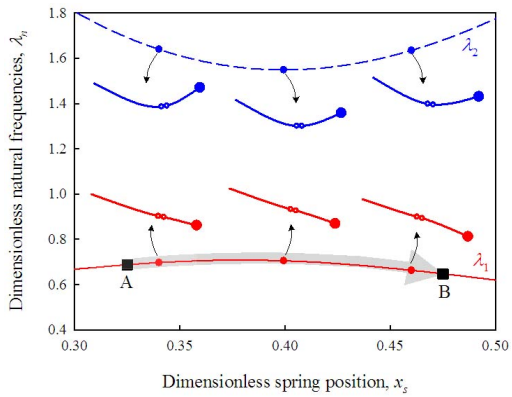

Fig. 15. First and second mode shapes for variation in the spring position when $M = 0.4$, $k = 3 \times 10^3$, and $a = 0.05$.

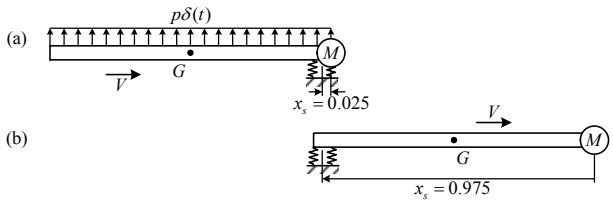

Fig. 16. Motion of a beam with a tip mass moving in the axial direction: (a) Initial position; (b) final position.

translates to the right with constant speed $V = 0.01$, and then is located on the right side of the spring position, as shown in Fig. 16(b). It is assumed that the dimensionless initial and final spring position are given by $x_s = 0.025$ and 0.975, respectively, and the dimensionless spring gap is $a = 0.05$. In addition, a dimensionless impulsive load, which is given by $p\delta(t)$ with $p = -1$, is applied to the beam when the beam is at the initial position.

Consider the dynamic responses of the beam for $M = 0.4$, $k = 100.6 \times 10^3$, $c_d = 0$ and $a = 0.05$. The dynamic responses of the dimensionless transverse displacements are presented in Fig. 17, where the horizontal axis represents the dimensionless spring position that can be transformed to dimensionless time. The transverse displacement in this figure is computed by the horizontal component of the position vector given by Eq. (1). The transverse displacements at the left and right ends (i.e., at $x = -1/2$ and $1/2$) are plotted in Figs. 17(a) and (b), respectively. As the beam translates to the right, the vibration amplitude and period of the left end decrease, as shown in Fig. 17(a), while in Fig. 17(b), vibration hardly occurs at the right end (i.e., tip mass position).

Using the STFT, the frequency spectra are obtained by the dynamic response at the interval between the vertical solid lines (i.e., the dimensionless spring position $0.30 < x_s < 0.35$) and the interval between the vertical dashed lines (i.e., the dimensionless spring position $0.45 < x_s < 0.50$), as shown in Fig. 17, and the frequency spectra are plotted in Fig. 18. Figs. 18(a) and (b) represent the frequency spectra for the dynamic response at the left and right ends, and the solid and dashed lines are the frequency spectra for the dynamic response corresponding to the spring positions $0.30 < x_s < 0.35$ and $0.45 <$

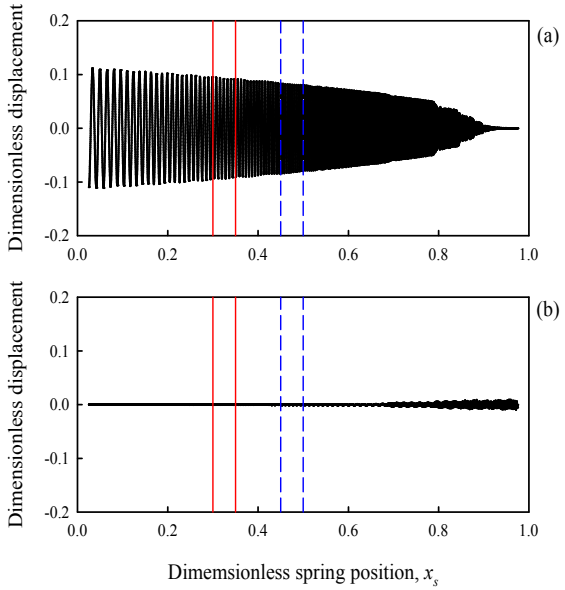

Fig. 17. Dynamic responses of the transverse displacements versus the spring position when $M = 0.4$, $k = 100.6 \times 10^3$, $c_d = 0$, and $a = 0.05$: (a) at the left end (i.e., at $x = -0.5$); (b) at the right end (i.e., at $x = 0.5$).

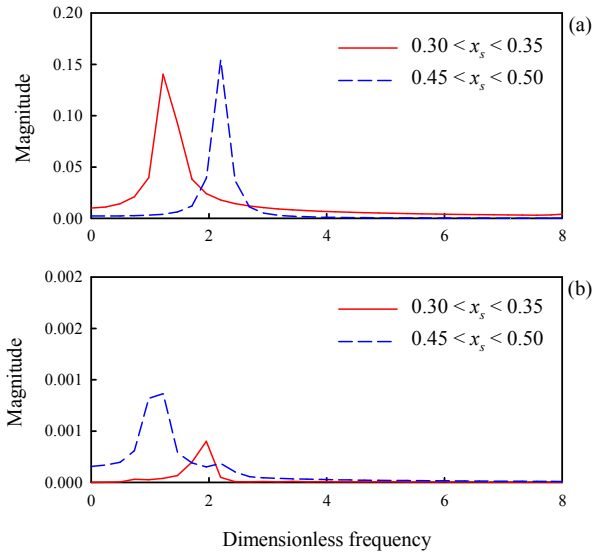

Fig. 18. Frequency spectra of the dynamic responses, shown in Fig. 17, during the intervals of $0.30 < x_s < 0.35$ and $0.45 < x_s < 0.50$: (a) At the left end (i.e., at $x = -0.5$); (b) at the right end (i.e., at $x = 0.5$).

$x_s < 0.50$, respectively. Comparing Figs. 18(a) and (b), it is observed that the peaks in Fig. 18(a) are much larger than the peaks in Fig. 18(b). This is because the vibration amplitude at the tip mass position is rather smaller than the vibration amplitude at the left end. It can be seen in Fig. 18(a) that the frequency spectrum for $0.30 < x_s < 0.35$ has a peak at the dimensionless frequency of 1.2209 and the spectrum for $0.45 < x_s < 0.50$ has a peak at the dimensionless frequency of 2.1977. These peak frequencies are very close to the dimensionless natural frequencies of 1.2341 and 2.0382 for points A and B

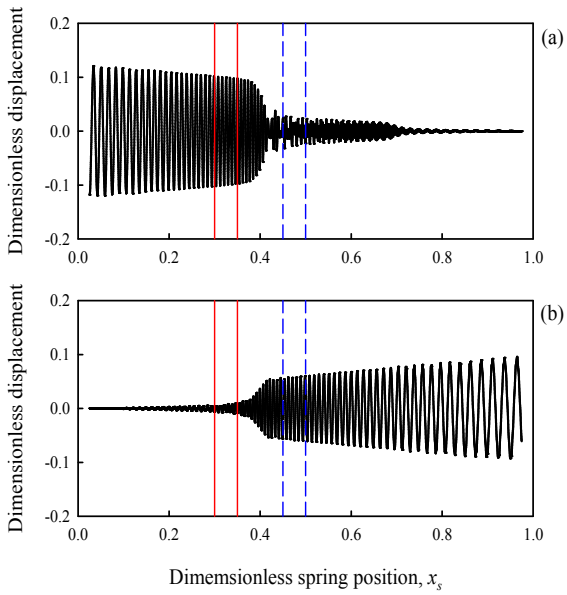

Fig. 19. Dynamic responses of the transverse displacements versus the spring position when $M = 0.4$, $k = 30 \times 10^3$, $c_d = 0$, and $a = 0.05$: (a) At the left end (i.e., at $x = -0.5$); (b) at the right end (i.e., at $x = 0.5$).

shown in Fig. 13, where points A and B represent the dimensionless natural frequencies at the midpoints of intervals for $0.30 < x_s < 0.35$ and $0.45 < x_s < 0.50$, respectively. This means that the beam vibrates by a mode shape corresponding to the first natural frequency, λ_1, when the spring position is $0.30 < x_s < 0.35$, and it vibrates by a mode shape corresponding to the second natural frequency, λ_2, when the spring position becomes $0.45 < x_s < 0.50$. This is because the first mode shape in the region $0.30 < x_s < 0.35$ exchanges to the second mode shape in the region $0.45 < x_s < 0.50$, along the shaded thick line in Fig. 13.

When the dimensionless tip mass and dimensionless gap between the two springs are fixed at $M = 0.4$, $c_d = 0$ and $a = 0.05$, and the dimensionless spring constant is reduced to $k = 30 \times 10^3$, the transverse displacements at the right and left ends of the beam are computed and presented in Fig. 19, where Figs. 19(a) and (b) represent the transverse displacements of the beam at the left and right ends, respectively. As shown in these figures, the vibration amplitudes at both ends change significantly near the dimensionless spring position $x_s = 0.3993$. This spring position corresponds to the veering position, where the first and second natural frequencies are closest in Fig. 14. It can also be seen that the transverse displacement at the right end in Fig. 19(b) differs from that in Fig. 18(b).

The frequency spectra for the dynamic responses in Fig. 19 are presented in Fig. 20. In Fig. 20(a), the frequency spectrum for $0.30 < x_s < 0.35$ has a peak at the dimensionless frequency of 1.2209, which is close to the dimensionless first natural frequency $\lambda_1 = 1.1616$ for point A in Fig. 14, while the frequency spectrum for $0.45 < x_s < 0.50$ has two dimensionless peak frequencies of 0.9768 and 2.1977; these peak frequencies are close to the dimensionless natural frequencies $\lambda_1 = 1.1024$

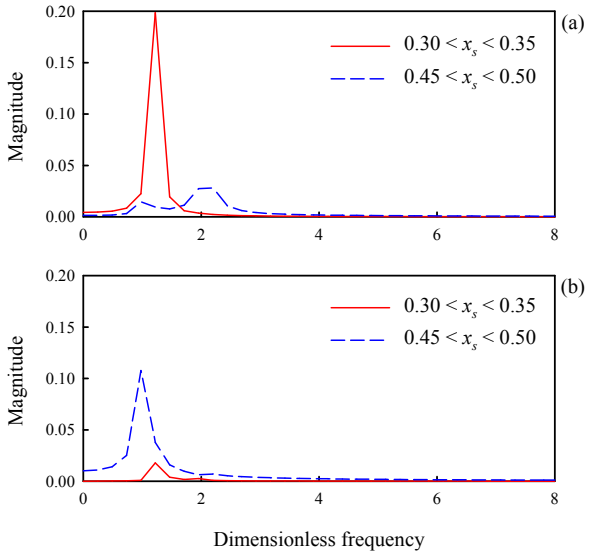

Fig. 20. Frequency spectra of the dynamic responses, shown in Fig. 19, during the intervals of 0.30 < x_s < 0.35 and 0.45 < x_s < 0.50: (a) At the left end (i.e., at x = -0.5); (b) at the right end (i.e., at x = 0.5).

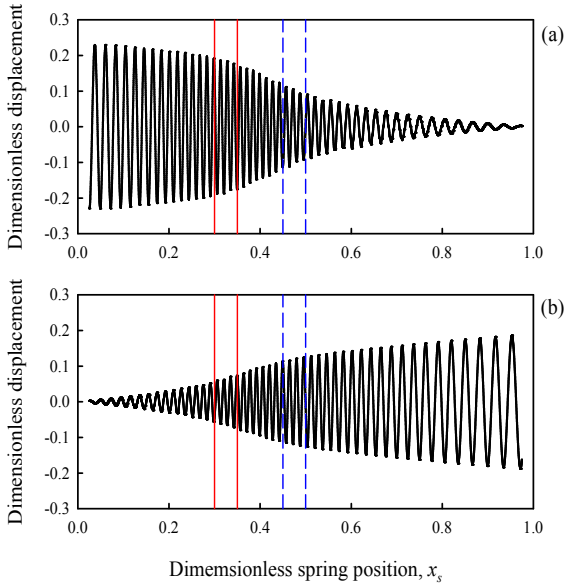

Fig. 21. Dynamic responses of the transverse displacements versus the spring position when M = 0.4, k = 3 × 10^3, c_d = 0, and a = 0.05: (a) At the left end (i.e., at x = -0.5); (b) at the right end (i.e., at x = 0.5).

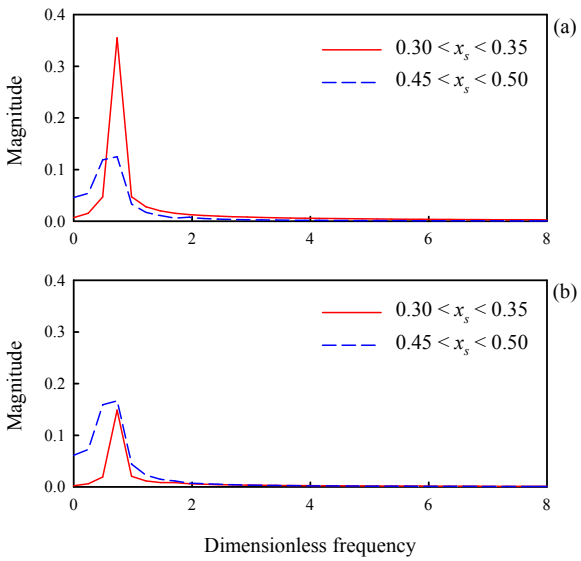

Fig. 22. Frequency spectra of the dynamic responses, shown in Fig. 21, during the intervals of 0.30 < x_s < 0.35 and 0.45 < x_s < 0.50: (a) At the left end (i.e., at x = -0.5); (b) at the right end (i.e., at x = 0.5).

and λ_2 = 1.9216, which correspond to points B and C, shown in Fig. 14. As described by the shaded arrow curves in Fig. 14, this indicates that the vibration with the first natural frequency λ_1 is transformed to vibrations with the first and second natural frequencies λ_1 and λ_2 while the beam moves from the position x_s = 0.3 to the position x_s = 0.5.

In Fig. 20(b), the frequency spectra for the displacement at the tip mass position are shown. The dimensionless peak frequencies are 1.2209 for 0.30 < x_s < 0.35 and 0.9768 for 0.45 < x_s < 0.50. These peak frequencies are similar to the first dimensionless natural frequencies corresponding to points A and B in Fig. 14. By comparing the frequency spectra for 0.45 < x_s < 0.50 at the left (Fig. 20(a)) and right ends (Fig. 20(b)), two peak frequencies are observed in Fig. 20(a) while Fig. 20(b) shows only one peak frequency. This can be explained similarly to Fig. 14. In Fig. 14, the mode shapes for the natural frequencies are near points B and C; the first mode shape near point B has a large deflection in the tip mass position, while the second mode shape near point C does not have a deflection in the tip mass position. Thus, only the first mode can be represented in the dynamic response at the tip mass position.

We further reduce the dimensionless spring constant to k = 3 × 10^3 and observe the displacements at the two ends of the beam. The dynamic responses at the left and right ends of the beam are plotted in Fig. 21. The vibration period in Fig. 21 is larger than those in Figs. 17 and 19. Additionally, it can be seen that the amplitude at the left end decreases gradually, while the amplitude at the tip mass position increases gradually.

To investigate the vibration frequencies for 0.30 < x_s < 0.35 and 0.45 < x_s < 0.50, the frequency spectra of the dynamic response (in Fig. 21) are plotted in Fig. 22. In this figure, it can be seen that the dimensionless peak frequencies at the left and right ends are 0.7326 and they are almost the same. However, in fact, these peak frequencies differ and the observation occurs due to a resolution problem with the STFT. These peak frequencies are close, compared with the natural frequencies for points A and B in Fig. 15, which are 0.6878 and 0.6476, respectively. Since the first and second natural frequencies are far from each other in Fig. 15, the corresponding modes do not interact with each other. Thus, the first mode shape remains as the beam translates to the right.

To observe the effect of structural damping, the dynamic re-

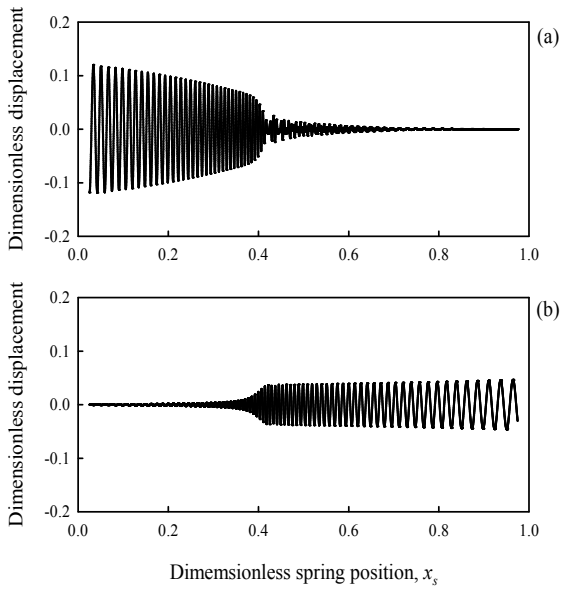

Fig. 23. Dynamic responses of the transverse displacements versus the spring position when $M = 0.4$, $k = 30 \times 10^3$, $c_d = 0.5$, and $a = 0.05$: (a) At the left end (i.e., at $x = -0.5$); (b) at the right end (i.e., at $x = 0.5$).

sponses of the transverse displacements are examined when the beam possesses structural damping. Fig. 23 shows the dynamic responses of the transverse displacements versus the dimensionless spring position when $M = 0.4$, $k = 30 \times 10^3$, $c_d = 0.5$ and $a = 0.05$. The physical parameters used to plot Figs. 19 and 23 are the same except the structural damping coefficient: $c_d = 0$ for Fig. 19 and $c_d = 0.5$ for Fig. 23. Comparing Figs. 19 and 23, there is no change in the spring position ($x_s = 0.3993$) where the vibration amplitudes change significantly. However, the vibration amplitudes when $c_d = 0.5$ (Fig. 23) are considerably reduced comparing to the amplitudes when $c_d = 0$ (Fig. 19). Therefore, it may be concluded that the structural damping influences only the magnitude of vibration.

Finally, it is valuable to show the values of the veering natural frequencies and positioning accuracy of a manipulator with real (or dimensional) system parameters. For this purpose, the following dimensional parameters, which were also adopted in Refs. [5, 9, 11], are used: $L = 1$ m, $A = 1.4661\times10^{-3}$ m^2, $I = 1.1073\times10^{-8}$ m^4, $E = 6.8335\times10^{10}$ N/m^2, $\rho = 2738.6$ kg/m^3, $c_d = 0$, $a = 0.05$ m, $M = 1.6060$ kg and $x_s = 0.3993$ m. These values correspond to the dimensionless parameters of $M = 0.4$, $c_d = 0$, $a = 0.05$ and $x_s = 0.3993$. The three dimensional spring constants of $k = 7.61\times10^7$, 2.27×10^7 and 2.27×10^6 N/m can be transformed to the dimensionless constants of $k = 100.6\times10^3$, 30×10^3 and 3×10^3, respectively, which are used in the above discussions.

At the veering position of $x_s = 0.3993$ m, the dimensional veering frequencies when $k = 7.61\times10^7$ N/m^2 are $\omega_1 = 3.402$ Hz and $\omega_2 = 3.414$ Hz (Fig. 13), the veering frequencies when $k = 2.27\times10^7$ N/m are $\omega_1 = 3.015$ Hz and $\omega_2 = 3.407$ Hz (Fig. 14), and the frequencies when $k = 2.27\times10^6$ N/m are $\omega_1 = 1.544$ Hz and $\omega_2 = 3.385$ Hz (Fig. 15). The maximum residual vibration amplitudes of the tip mass, which represent the position accuracy of a manipulator, are 0.006 m for $k = 7.61\times10^7$ N/m (Fig. 17(b)), 0.061 m for $k = 2.27\times10^7$ (Fig. 19(b)), and 0.162 m for $k = 2.27\times10^6$ (Fig. 21(b)). The dimensional veering frequencies and maximum residual vibration amplitudes for the three spring constants are presented in Table 3.

Table 3. Dimensional veering natural frequencies at $x_s = 0.3993$ m and maximum residual vibration amplitude of the tip mass.

Spring constant, k (N/m)	Veering natural frequencies, ω_n (Hz)		Maximum residual vibration amplitude (m)
	ω_1	ω_2	
7.61×10^7	3.402	3.414	0.006
2.27×10^7	3.015	3.407	0.061
2.27×10^6	1.544	3.385	0.162

7. Conclusions

In this study, the vibrations of a moving beam with a tip mass are analyzed when the beam is supported by springs. Considering the tip mass effect, the coupled rigid-body and flexible equations of motion were derived. The equations of motion were transformed into the weak forms, and then discretized equations were obtained using the Galerkin method. The dynamic characteristics and responses were investigated with variation in the spring position/constant, and tip mass.

The results of this paper may be summarized as follows:

(1) The natural frequency loci veering was analyzed, and it was found that the occurrence and characteristics of the veering are affected by the spring position, spring constant, and tip mass value.

(2) The mode localization and mode exchange are closely related to the natural frequency veering. In particular, for a specific spring constant, where the two lowest natural frequencies are close around the veering region, mode exchange and localization occur regardless of the tip mass and spring position values.

(3) Transverse displacements are influenced by the veering distance of the natural frequencies for the spring constant. As the veering distances become closer, the vibration of the axially moving beam in the first mode exchanges to the second mode, whereas as the veering distances become further apart, the axially moving beam vibrates only in the first mode.

References

[1] P. K. C. Wang and J. D. Wei, Vibrations in a moving flexible robot arm, *Journal of Sound and Vibration*, 116 (1) (1987) 149-160.

[2] M. Stylianou and B. Tabarrok, Finite element analysis of an axially moving beam, part 1: time integration, *Journal of Sound and Vibration*, 178 (4) (1994) 433-453.

[3] L. H. Wang, Z. D. Hu, Z. Zhong and J. W. Ju, Hamiltonian dynamic analysis of an axially translating beam featuring

time-variant velocity, *Acta Mechanica*, 206 (3-4) (2009) 149-161.
[4] Y. Matsuzaki, Y. Taki and M. Toyama, Vibration of a cantilevered beam during deployment and retrieval: analysis and experiment, *Smart Material and Structures*, 4 (4) (1995) 334-339.
[5] B. O. Al-Bedoor and Y. A. Khulief, An approximate analytical solution of beam vibrations during axial motion, *Journal of Sound and Vibration*, 192 (1) (1996) 159-171.
[6] B. O. Al-Bedoor and Y. A. Khulief, Vibrational motion of an elastic beam with prismatic and revolute joints, *Journal of Sound and Vibration*, 190 (2) (1996) 195-206.
[7] K. Zhu and J. Chung, Nonlinear lateral vibrations of a deploying Euler-Bernoulli beam with a spinning motion, *International Journal of Mechanical Sciences*, 90 (2015) 200-212.
[8] R. F. Fung, P. Y. Lu and C. C. Tseng, Non-linearly dynamic modelling of an axially moving beam with a tip mass, *Journal of Sound and Vibration*, 218 (4) (1998) 559-571.
[9] J. R. Chang, W. J. Lin, C. J. Huang and S. T. Choi, Vibration and stability of an axially moving Rayleigh beam, *Applied Mathematical Modelling*, 34 (6) (2010) 1482-1497.
[10] L. H. Wang, Z. D. Hu, Z. Zhong and J. W. Ju, Dynamic analysis of an axially translating viscoelastic beam with an arbitrarily varying length, *Acta Mechanica*, 214 (3-4) (2010) 225-244.
[11] S. Park, H. H. Yoo and J. Chung, Vibrations of an axially moving beam with deployment or retraction, *AIAA Journal*, 51 (3) (2013) 686-696.
[12] S. Park, H. H. Yoo and J. Chung, Eulerian and Lagrangian descriptions for the vibration analysis of a deploying beam, *Journal of Mechanical Science and Technology*, 27 (9) (2013) 2637-2643.
[13] Y. C. Duan, J. P. Wang, J. Q. Wang, Y. W. Liu and F. Shao, Theoretical and experimental study on the transverse vibration properties of an axially moving nested cantilever beam, *Journal of Sound and Vibration*, 333 (13) (2014) 2885-2897.
[14] B. Kim and J. Chung, Residual vibration reduction of a flexible beam deploying from a translating hub, *Journal of Sound and Vibration*, 333 (16) (2014) 3759-3775.
[15] E. Ozkaya and M. Pakdemirli, Group-theoretic approach to axially accelerating beam problem, *Acta Mechanica*, 155 (1-2) (2002) 111-123.
[16] T. Yang, B. Fang, X. D. Yang and Y. Li, Closed-form approximate solution for natural frequency of axially moving beams, *International Journal of Mechanical Sciences*, 74 (2013) 154-160.
[17] M. Rezaee and S. Lotfan, Non-linear nonlocal vibration and stability analysis of axially moving nanoscale beams with time-dependent velocity, *International Journal of Mechanical Sciences*, 96-97 (2015) 36-46.
[18] C. Pierre, D. M. Tang and E. H. Dowell, Localized vibrations of disordered multispan beams: theory and experiment, *AIAA Journal*, 25 (9) (1987) 1249-1257.
[19] C. Pierre, Mode localization and eigenvalue loci veering phenomenon in disordered structures, *Journal of Sound and Vibration*, 126 (3) (1988) 485-502.
[20] S. D. Lust, P. P. Friedmann and O. O. Bendiksen, Mode localization in multispan beams, *AIAA Journal*, 31 (2) (1993) 348-355.
[21] A. A. N. Al-Jawi, C. Pierre and A. G. Ulsoy, Vibration localization in dual-span axially moving beams, part 1: formulation and results, *Journal of Sound and Vibration*, 179 (2) (1995) 243-266.
[22] M. H. Ghayesh, Stability and bifurcations of an axially moving beam with an intermediate spring support, *Nonlinear Dynamics*, 69 (1-2) (2012) 193-210.
[23] M. H. Ghayesh, M. Amabili and M. P. Paidoussis, Nonlinear vibrations and stability of an axially moving beam with an intermediate spring support: two-dimensional analysis, *Nonlinear Dynamics*, 70 (1) (2012) 335-354.
[24] O. R. Jaiswal and R. N. Iyengar, Dynamic response of a beam on elastic foundation of finite depth under a moving force, *Acta Mechanica*, 96 (1-4) (1993) 67-83.
[25] S. Park and J. Chung, Dynamic analysis of an axially moving finite-length beam with intermediate spring supports, *Journal of Sound and Vibration*, 333 (24) (2014) 6742-6759.
[26] J. Chung and G. M. Hulbert, A time integration algorithm for structural dynamics with improved numerical dissipation: the generalized-alpha method, *Journal of Applied Mechanics*, 60 (2) (1993) 371-375.

Jaewon Kim received his B.S. degree in 2012 from the Department of Mechanical Engineering at Hanyang University. He is currently a Ph.D. candidate in the Department of Mechanical Engineering at Hanyang University. His research interests are the dynamics of robot manipulator and the vibration and noise reductions of rotating machines and vehicles.

Jintai Chung received his B.S. and M.S. degrees from the Department of Mechanical Engineering at Seoul National University in 1984 and 1986, respectively. He obtained his Ph.D. degree from the Department of Mechanical Engineering at University of Michigan, Ann Arbor in 1992. He is currently a Professor in the Department of Mechanical Engineering at Hanyang University. His research interests are vibration and noise reductions of rotating machines, vehicles and home appliances.